



HAL
open science

Substituted effect of Al³⁺ on structural, optical, magnetic and photocatalytic activity of Ni ferrites

A. Lassoued, M.S. Lassoued, Brahim Dkhil, S. Ammar, A. Gadri

► To cite this version:

A. Lassoued, M.S. Lassoued, Brahim Dkhil, S. Ammar, A. Gadri. Substituted effect of Al³⁺ on structural, optical, magnetic and photocatalytic activity of Ni ferrites. *Journal of Magnetism and Magnetic Materials*, 2019, 476, pp.124-133. 10.1016/j.jmmm.2018.12.062 . hal-02109059

HAL Id: hal-02109059

<https://centralesupelec.hal.science/hal-02109059>

Submitted on 13 Oct 2021

HAL is a multi-disciplinary open access archive for the deposit and dissemination of scientific research documents, whether they are published or not. The documents may come from teaching and research institutions in France or abroad, or from public or private research centers.

L'archive ouverte pluridisciplinaire **HAL**, est destinée au dépôt et à la diffusion de documents scientifiques de niveau recherche, publiés ou non, émanant des établissements d'enseignement et de recherche français ou étrangers, des laboratoires publics ou privés.

Substituted effect of Al³⁺ on structural, optical, magnetic and photocatalytic activity of Ni ferrites

Abdelmajid Lassoued ^{a, b*}, Mohamed Saber Lassoued ^a, Brahim Dkhil ^b,

Salah Ammar ^a and Abdellatif Gadri ^a

^a *Unité de Recherche Electrochimie, Matériaux et Environnement UREME (UR17ES45),
Faculté des Sciences de Gabès, Université de Gabès, Cité Erriadh, 6072 Gabès, Tunisie.*

^b *Laboratoire Structures, Propriétés et Modélisation des Solides CentraleSupélec,
CNRS-UMR8580, Université Paris-Saclay 91190 Gif-sur-Yvette, France.*

*: *Corresponding author e-mail address: Labdelmajid@yahoo.com*

Abstract

Al-substituted nickel ferrite NiAl_xFe_{2-x}O₄, where x = (0.00, 0.05, 0.10 and 0.15) synthesized through chemical co-precipitation method were investigated for their structural, morphological, optical and magnetic characterization. Al³⁺ substitution plays a significant role in the properties of the ferrite nanoparticles. The TGA showed three mass losses, whereas DTA resulted in three endothermic peaks. Rietveld refined XRD revealed the development of single phase cubic spinel with crystallite sizes around 28 - 36 nm for aluminum substituted samples. TEM and SEM analysis showed the monodispersion and cubic-like nanostructure. The room temperature infra-red spectra showed the features of higher and lower energy bands detected at $\nu_1 \sim 589\text{-}595\text{ cm}^{-1}$ and $\nu_2 \sim 405\text{-}409\text{ cm}^{-1}$, respectively corresponded to octahedral vibration (O-band) and tetrahedral (T-band) complexes that also verify the creation of spinels ferrites. The Raman spectra showed five Raman active modes ($A_{1g} + E_g + 3T_{2g}$) which are estimated in the spinel structure. The optical study showed that the compounds have an

optical band gap between 1.60 and 1.89 eV. Mössbauer spectra elucidate the nature of the phases and cation distribution. From the hysteresis loop, it is clear that the synthesized samples can be control, for the $\text{NiAl}_x\text{Fe}_{2-x}\text{O}_4$ nanoferrites. The photocatalytic activity of Al-substituted nickel ferrite were studied based on the degradation of methyl orange as a model compound, where the results showed that $\text{NiAl}_{0.15}\text{Fe}_{1.85}\text{O}_4$ a good photocatalytic activity.

Keywords:

Spinel ferrites ($\text{NiAl}_x\text{Fe}_{2-x}\text{O}_4$); Co-precipitation; Substitution; Magnetic parameters; Photocatalysis.

1. Introduction

For half a century, nanotechnologies have covered a large number of technological fields whose common denominator is the nanometric size of structures. This is a major theme of research for both basic science and applications, relying heavily on the development of nanomaterials [1-3]. Spinel ferrites (MFe_2O_4) are one of the most important classes of magnetic materials. They already have many fields of application, because of their original magnetic properties, their low cost of production, compared to better known magnetic materials based on precious metals [4-6]. The most common applications are magnetic recording, and use as a massive component for power and permeability applications [7-12]. Spinel is a generic term for a crystalline structure of the general formula $\text{A}^{2+}\text{B}_2^{3+}\text{O}_4$ (A and B representing metal cations) [13, 14]. The crystallographic structure adopts the space group belonging to the cubic system, Fd-3m (No. 227 in the international tables) with a mesh parameter of the order of 8.4 Å. This structure is constructed from the cubic compact arrangement of oxygen ions within which the actions are distributed among the tetrahedral sites (Th) which will be designated by the notation A, and the octahedral sites (Oh) which will be these cubic faces-centered cubicles defined by the oxygens contain 32 octahedral sites, 16

of which are occupied, and 64 tetrahedral sites, 8 of which are occupied. To describe the structure, divide the parameter mesh into 8 cubes called an octant of edge $a / 2$. The magnetism of spinel nanoferrites is derived from super exchange between cations in tetrahedral (A-site) and octahedral (B-site) including A–B exchange, B–B exchange and A–A exchange. Therefore, the magnetic parameters of spinel are associated to the distribution species of cations in A-site and B-site. The properties of spinel ferrites are influenced by method used for the synthesis, chemical composition and cation distribution [15, 16]. Many methods have been developed to prepare nanocrystallite AB_2O_4 namely organic gel-thermal decomposition method, sol–gel auto-combustion method, co-precipitation method, gel-assistant hydrothermal route, hydrothermal method, thermolysis, citric acid combustion method, self-propagating, wet chemical coprecipitation technique, microemulsion and polymer assisted coprecipitation method [17–30]. Chemical co-precipitation method is mostly attractive thanks to its low cost, short preparation time, high homogeneity and purity, relatively low reaction temperature and well-crystallized product.

Al-substituted Ni ferrites have specific properties with respect to ferrite nickel, for example: the addition of Al inhibits particle growth and improves the mechanical strength of ferrites [31]. In addition, the addition of Al^{3+} increases the resistivity and thus decreases the dielectric losses, and also decreases the saturation magnetization. In addition, the addition of Al^{3+} reduces magnetic coercivity and causes ferrite to become softer for some high frequency applications.

In this work we investigate the effect of aluminum (Al) substitution on the structural, morphological and magnetic properties of prepared by co-precipitation method. We have used co-precipitation method which stands for a simple procedure to synthesize spinel ferrites nanoparticles. The synthesized compounds are well characterized for their structural, morphological, optical and magnetic properties by various characterization techniques such as

Thermo Gravimetric Analysis (TGA), Differential Thermal Analysis (DTA), X-ray diffraction (XRD) with Rietveld refinement technique, Transmission Electron Microscopy (TEM), Scanning Electron Microscopy (SEM), Fourier Transform Infra-Red (FT-IR) spectroscopy, Raman spectroscopy, Ultraviolet-Visible (UV-Vis) analysis, Mössbauer spectroscopy and Vibrating Sample Magnetometer (VSM).

2. Experimental

2.1. Materials

Chemicals with high purity were purchased from Aldrich and used without further purification. Deionized distilled water was used for all the experiments. The raw materials are: (FeCl₃, 6H₂O), (NiCl₂, 6H₂O), (AlCl₃, 6H₂O), (NaOH), acid oleic (C₁₈H₃₄O₂) and ethanol (C₂H₆O).

2.2. Synthesis of NiAl_xFe_{2-x}O₄ nanoparticles

Nanosized (NiAl_xFe_{2-x}O₄), where x = (0, 0.05, 0.10, 0.15) particles were synthesized by facile co-precipitation method. The starting materials nickel chloride hexahydrate (NiCl₂,6H₂O), aluminum chloride hexahydrate (AlCl₃,6H₂O) and iron chloride hexahydrate (FeCl₃,6H₂O) were weighed in a well determined stoichiometric ratio, **and dissolved separately for 15 minutes in order to have an apparent and homogeneous solution**. Then, 3M of the mineralizer, NaOH was added in the admixing solution in order to maintain pH 11 and a few drops of oleic acid as a surfactant and coating material [32]. The solution was maintained at an ambient temperature of 80°C for 3 hours to obtain brown precipitate. The precipitate thus obtained was magnetically separated by washing several times with deionized distilled water and ethanol and the byproduct was dried overnight at 80 °C under air atmosphere in an oven. Then the dried powder was ground well and sintered at the temperature 700 °C for 6 h in a furnace.

2.3. Characterization

The thermal behavior was evaluated by Thermo Gravimetric (TGA) and Differential Thermal Analysis (DTA) in the air with TGA Q500 TA instrument. The X-ray diffraction patterns of the compounds were identified by German Bruker D2 PHASER X-ray diffractometer with $\text{CuK}\alpha$ radiation (1.5418 Å) as a source. The intensity data were collected over the range of 20°–80° using a step scan mode (0.001°/s). The data were processed to analyze all of the samples using the computer Program FullProf.2k (Version 4.30—Apr 2008-ILL JRC) in the Rietveld method for structure refinement. The TEM micrographs were obtained on a JEOL 2011 transmission electron microscope with an accelerating voltage of 200 kV. Micro structural characteristics such as morphology and particle size of compounds were analyzed through scanning electron microscope (SEM) with KYKY-EM3200, 25KV type. Fourier Transform Infra-Red (FT-IR) spectra of samples were explored through a NICOLET IR200 FT-IR spectrometer with transmission from 4000 to 400 cm^{-1} . The Raman spectra were composed using a Renshaw in Via Raman microscope with a 50x objective coupled to a 632.80 nm He-Ne laser excitation source (Renshaw RL633). The Ultraviolet-Visible (UV-Vis) absorption of the compounds was recorded on SHIMADZU (UV-3101 PC) UV-Vis Spectrophotometer. The ^{57}Fe Mössbauer spectra were collected on a FAST Comtec Mössbauer system at room temperature, using a ^{57}Co (Pd) source and a conventional constant acceleration mode. Magnetization measurements were performed by the vibrating sample magnetometer (VSM).

2.4. Photocatalytic activity measurements

The photocatalytic activities of the $\text{NiAl}_x\text{Fe}_{2-x}\text{O}_4$ nanoparticles with $x = (0.00, 0.05, 0.10, \text{ and } 0.15)$ were analyzed based on the photodegradation of MO at room temperature. The solution was irradiated with visible medium pressure xenon lamp (150 W) under magnetic stirring. In a typical photocatalytic experiment, 0.1 g of the sample was dispersed in

100 mL of MO aqueous solution. Before applying the irradiation, the suspension was magnetically stirred for 30 min in the dark to ensure that an adsorption–desorption equilibrium was reached between the $\text{NiAl}_x\text{Fe}_{2-x}\text{O}_4$ nanoparticles and the aqueous dye solution. Samples of the solution were then collected from the reactor at regular intervals, before centrifuging and analyzing to determine the residual amounts of the dye after photo-irradiation using a UV-Vis spectrophotometer (Shimadzu UV-2450).

3. Results and discussion

3.1. Thermal behavior and phase analysis

The findings associated with formation and decomposition phase occurring during heat treatment of synthesized samples ($\text{NiAl}_{0.05}\text{Fe}_{1.95}\text{O}_4$) are in excellent agreement through Thermo Gravimetric Analysis and Differential Thermal Analysis (TGA and DTA) results. Thermal analyses were carried out from 37 to 700 °C. TGA of the synthesized compound was performed by heating the samples in air atmosphere at 10 °C/min. **Fig. 1** depicts the thermal analyses (TGA, DTA) for spinel ferrite ($\text{NiAl}_{0.05}\text{Fe}_{1.95}\text{O}_4$).

Fig. 1 shows there were three distinct mass losses: the first was 5.56 % and occurred gradually between [44 °C – 182 °C]. This is attributed to the removal of water existing on the surface of prepared compound. One endothermic peak at 99.82 °C was observed using DTA. The second mass loss of 3.04 % occurred at [182 °C – 540 °C], which is due to the combustible organic products (acid oleic ($\text{C}_{18}\text{H}_{34}\text{O}_2$)) present in our prepared sample. Through the use of DTA we recorded one endothermic peak at 186.28 °C. The third mass loss stands for a minor weight loss (1.38 %) occurring in the range of [540 °C – 650 °C], which is due to the transition phase of prepared samples. Furthermore, using DTA helped us find one endothermic peak in DTA at 656.02 °C. As can be seen from this figure, after 660 °C the curve becomes parallel with the temperature axis which emphasizes the high stability of

NiAl_{0.05}Fe_{1.95}O₄ nanoparticles. There is no associated signal with the thermal processes of spinel ferrite nanoparticles in the TGA curve confirming their crystallization and phase transition.

3.2. X-ray diffraction analysis

Rietveld refined XRD patterns of NiAl_xFe_{2-x}O₄ (x = 0.00, 0.05, 0.10 and 0.15) are presented in **Fig. 2**. The formation of single phase cubic spinel structure similar to that of ICDD card (No. 86-2267) with space group Fd-3m was revealed by XRD patterns. The characteristic diffraction peaks of cubic structure as well as the crystal structure, both are maintained throughout aluminum substitution without any noticeable impurity peak [33, 34].

The analysis of XRD patterns reveals the nanocrystalline nature of the prepared samples. The average crystallite size, D_{XRD} , for each sample was estimated from the most intense peak (311) using Scherrer's formula [35-38].

$$D_{XRD} = \frac{k \lambda}{\beta \cos \theta} \quad [1]$$

Where k is the so-called shape factor (0.9), λ is the wavelength (0.15418 nm, CuK α), β is the full width at half maximum (FWHM), and θ is the diffraction angle. The average crystallite size was found to decrease from 36 nm to 28 nm with increasing Al³⁺ substituted. The XRD data were processed for Rietveld refinement of structure by FullProf.2k program. **Table 1** lists the Rietveld refinement parameters, crystallite size, and degree of crystallinity. The quality of the refinement was quantified by the corresponding figures of merit: profile residual R_p , weighted profile residual R_{wp} and goodness of fit χ^2 [39].

The lattice constant calculated by the Rietveld method and the values are listed in **Table 1** and was found to decrease from 8.280 to 8.223 Å with the increase in aluminum

concentration, which suggested the formation of a compositionally homogeneous solid solution and was found to be within the range of the lattice constants of NiFe_2O_4 . **Fig. 3a** clearly showed the continuous shift in 2θ with increasing Al concentration. It is also clear from **Fig. 3a** that the angle shifts towards higher values. This shift is attributed to decrease in lattice parameter.

The decrease in the lattice parameter with Al^{3+} ion substitution which is ascribed to the ionic radius difference between the substituted Al^{3+} (0.051 nm) and the displaced Fe^{3+} (0.064 nm) ions which is in accordance with Vegard's law [40]. The variation of lattice constant with Al^{3+} substitution inevitably supports the occupancy of the Al ions into the host Ni ferrite lattice. The variation of average crystallite size ' D_{XRD} ' and lattice parameter 'a' with the Al concentration is given in **Fig. 3b**.

3.3. Particle size and morphology measurements: TEM, SEM

The morphology of prepared ferrite nanopowders was determined through transmission electron microscope. Representative micrographs showing the surface morphology of $\text{NiAl}_x\text{Fe}_{2-x}\text{O}_4$ ferrites with different Al-content are demonstrated in **Fig. 4a**. TEM studies indicated that the average particle size of Ni-Al ferrites decreases with the increase of Al^{3+} content. This leads to the fact that, as the Fe^{3+} ions are substituted by Al^{3+} ions, the potential changes in lattice parameter leads to the lattice strains. Consequently, internal stress is developed onto the ferrites compounds that hinders the particle growths. Thus, the particle sizes of the Al-substituted Ni ferrites are reduced [41].

Fig. 4b shows morphological pattern of the synthesized ferrites powder taken via scanning electron microscope. SEM images of $\text{NiAl}_x\text{Fe}_{2-x}\text{O}_4$ showed the crystalline nature of the prepared nanoparticles and provide such a type of agglomeration. Substitution effects on the structures and particles sizes were determined. The particle size and morphology of the

compounds seem to be uniform with somewhat agglomeration in the prepared samples which is unavoidable. **Fig. 4b** indicates cubic-shaped nanoparticles of $\text{NiAl}_x\text{Fe}_{(2-x)}\text{O}_4$. However, the mean crystalline size of the prepared ferrite was in the range of 28 – 37 nm. The size of nanoparticles decreased with the increased aluminum contents because the ionic radius of iron (0.64 Å) is higher than that of aluminum (0.51 Å).

3. 4. FT-IR spectra

The FT-IR analysis also supports the formation of single phase. $\text{NiAl}_x\text{Fe}_{2-x}\text{O}_4$, where ($x = 0.00, 0.05, 0.10, 0.15$) ferrite materials. **Fig. 5** shows FT-IR spectra of the Al substituted Ni nanoferrites in the frequency range of 400–800 cm^{-1} . Two major absorption bands labeled as ν_1 and ν_2 correspond to the vibrations of the tetrahedral sites (A-O-A bonds) and the octahedral sites (B-O-B bonds), respectively [42-44]. The higher wavenumber band (ν_1) for all the samples, shifted from 589 to 595 cm^{-1} and lower wavenumber (ν_2), shifted from 405 to 409 cm^{-1} with the increased Al concentration. These bands confirmed the spinel structure of the prepared ferrite nanoparticles [45]. The observed shift in the peaks is expected and is due to modification in the occupation of the cations in tetrahedral (A) and octahedral (B) sites. It is well known that, the change in bond length has an inverse relation to the band frequency shift. Therefore, such increase in the frequency of absorption is due to the decrease in tetrahedral and octahedral bond lengths.

3 .5. Raman spectroscopy

Raman spectra performed at room temperature in the frequency range of 200-900 cm^{-1} of as synthesized $\text{NiAl}_x\text{Fe}_{2-x}\text{O}_4$, where ($x = 0.00, 0.05, 0.10, 0.15$) ferrites samples are shown in **Fig.6**. These ferrites have cubic inverse spinel structure of type AB_2O_4 belonging to Fd-3m (O7h) space group with eight formula units per unit cell. Although the full unit cell contains 56 atoms (8 molecules per unit cell), only 14 atoms are in the asymmetric unit and therefore

42 vibrational modes are expected. According to group theory, the irreducible representations for the studied systems are as follows:

$$\Gamma_{\text{irred}} = A_{1g}(\text{R}) + E_g(\text{R}) + T_{1g} + 3T_{2g}(\text{R}) + 2A_{2u} + 2E_u + 5T_{1u}(\text{IR}) + 2T_{2u} \quad [2]$$

The presence of an inversion center in the centro-symmetrical space group $Fd3m$ implies mutual exclusion of Raman and IR activities for the same vibrational mode. There are five first-order Raman active modes $A_{1g} + E_g + 3T_{2g}$ [46, 47] and all these modes were observed at ambient conditions whereas only the T_{1u} type normal vibrations modes are infrared-active. T_{1g} , A_{2u} , E_u and T_{2u} symmetry vibrations are the silent ones. All the IR-active vibrations are triply degenerated. A is for one dimensional representation, E for two and T for three dimensional representations, g denotes the symmetry with respect to the center of inversion. A_{1g} describes symmetric stretch of oxygen atoms along Fe–O (or M–O) tetrahedral bonds, $T_{2g}(1)$: translatory movement of the whole tetrahedron (FeO_4), $T_{2g}(2)$: asymmetric stretch of Fe(M)–O bond, $T_{2g}(3)$ and E_g : asymmetric and symmetric bends of oxygen with respect to Fe, respectively. In order to determine the natural frequency of the Raman active modes of each sample, a least square fit with Lorentzian line shape was used to fit the Raman spectra. The thick smooth lines are fits to the Lorentzian functions. The bands corresponding to these modes are observed at ambient conditions in Raman spectrum of NiFe_2O_4 whose values are:

$$T_{2g}(1) = 213 \text{ cm}^{-1}, E_g = 337 \text{ cm}^{-1}, T_{2g}(2) = 488 \text{ cm}^{-1}, T_{2g}(3) = 574 \text{ cm}^{-1}, A_{1g} = 702 \text{ cm}^{-1}$$

These results are in good agreement with earlier reported data on NiFe_2O_4 spinel [48-50].

3.6. Diffuse reflectance spectroscopy (DRS) studies

To study the effect of change in the concentration of substitution (Al^{3+}) on the optical properties of aluminum doped NiFe_2O_4 semiconductor ferrite materials, the UV–Visible

diffuse reflectance measurement was carried out. The band gap energy can be approximately calculated from the optical reflectance data by using the following equation [51-55]:

$$(\alpha h\nu)^n = A (h\nu - E_g) \quad [3]$$

Where α is the absorption coefficient, A is constant, $h\nu$ is the energy of light and n is a constant depending on the nature of the electron transition [56]. Spinel ferrites (MFe_2O_4) has a direct band gap ($n=2$) [57]. **Fig. 7a** shows the plot of $(\alpha h\nu)^2$ versus $h\nu$. The energy gap can be obtained from the intercept of the linear absorption edge part with the energy axis. When $(\alpha h\nu)^2$ is zero, the photon energy is E_g . The optical band gap of spinels ferrite was observed in **Table 2**. It is noted that the optical band gap increases with the increase in Al content (**Fig. 7b**).

3.7. Mössbauer investigations

The Mössbauer spectra recorded at 300 K for the samples $x = 0.0, 0.05, 0.1$ and 0.15 are shown in **Fig. 8**. Mossbauer's parameters are collated in the **Table 3**. For $x = 0.0-0.1$ the spectra exhibit a superposition of two Zeeman sextets (magnetic components) [58], one due to the Fe^{3+} ions at the tetrahedral (A) and the other due to Fe^{3+} ions at the octahedral (B) sites. The spectrum for $x = 0.15$ was fitted the coexistence of magnetic as well as superparamagnetic components. The intensity of the central superparamagnetic doublet with respect to the magnetic sextets increases with increasing x values. Thus, as the content of non-magnetic Al^{3+} increases in $NiAl_xFe_{2-x}O_4$ system, the magnetic coupling (ferrimagnetism) is weakened from that of Ni ferrites ($x = 0$) to that of superparamagnetic composition ($x = 1.0$).

3.8. Magnetic properties

The magnetization versus applied field for different samples is shown in **Fig. 9a**. The values of coercivity (H_c), saturation magnetization (M_s) and remanent (M_r) of all the samples are extracted from these loops and tabuled in **Table 4**.

It is clear from **Fig. 9b** that the magnetization decreases with increasing Al content [59]. This effect can be explained by the following reasons.

Firstly, particle size: as the Al content increases the particle size decreases (**Fig.3b**). The existence of some degree of the spin canting in the whole volume of the nanoparticles and the disordered surface/dead layer at the surface can explain the decrease of the saturation magnetization.

Secondly, weakening of A–B interactions: as Al replaces some of the Fe ions, the magnetic coupling weakens because the Al ion itself does not carry the magnetic moment ($1s^2 2s^2 2p^6$). The mechanism of the substitution can be described by replacing Ni cations with non-magnetic Al cations which prefer the octahedral sites. Then, it leads to the weakening of the A–B interactions and thus leads to a disturbance of the spin ordering, causing the destabilization of the magnetic ordering. In the spinel structure Ni^{2+} ions have a very strong preference for octahedral sites. Also, Fe^{3+} ions have a stronger preference for the tetrahedral sites as compared to the octahedral sites.

Fig. 9b exhibits the magnetic coercivity as a function of Al content. The reduction in magnetic coercivity with the Al content can be described as follows

a) Particle size. When the grain size reaches below the critical single domain size the magnetic coercivity decreases with the grain size ($H_c \propto D^6$).

b) Magneto crystalline anisotropy. In addition to the Ni ($[Ar] 4s^0 3d^8$) migration, another reason is the angular momentum of the Al ion. Al^{3+} has a zero angular momentum ($l=0$) and does not contribute to magneto-crystalline anisotropy. As the Al ion ($l=0$) replaces some of the Ni ions ($d^8, l \neq 0$), the spin–orbit coupling weakens because Al^{3+} itself does not carry the angular momentum; consequently, the magnetic anisotropy and magnetic coercivity will decrease.

3.8. Photocatalytic Experiments

Photocatalytic experiments were carried out in the presence of the as-prepared (NiAl_xFe_{2-x}O₄) with (x = 0.00, 0.05, 0.10, 0.15) nanostructures as photocatalyst and methyl orange dye as organic pollutants under visible irradiation (Fig. 10a). The dye degradation percent was calculated as follows [60]:

$$\text{Percentage of degradation} = (1 - A_t / A_0) * 100 \quad [4]$$

Where A₀ and A_t are the absorbance value of the solution at 0 and t min, respectively.

Blank experiments under Visible illumination without the nanoparticles were first bearded out to rationalize the photocatalytic activity of the (NiAl_xFe_{2-x}O₄) nanoparticles. This, blank experiment result Indicated that MO could not be decomposed without the photocatalyst. By contrast introduction of the photocatalysts induced the rapid degradation of MO. (NiAl_xFe_{2-x}O₄) nanoparticles gave rise to higher photocatalytic activities than NiFe₂O₄. The (NiAl_{0.15}Fe_{1.85}O₄) photocatalyst led to the highest degradation rate, i.e. 76.2 % after 140 min of visible light irradiation, whereas NiFe₂O₄, NiAl_{0.05}Fe_{1.95}O₄ and NiAl_{0.10}Fe_{1.90}O₄ samples yielded decomposition rate of 62.67 %, 67.91 % and 74.12 % respectively (Fig. 10b). To study the kinetics of photocatalytic reactions, Langmuir- Hinshelwood model was investigated as follows [61]:

$$r = -dc/dt = Kkc / (1 + KA) \quad [5]$$

Where **r** is the rate of reaction (mol/L·min), **A** is the equilibrium concentration of the reagent (mol/L), **t** is the time (min), **k** is the rate constant (L/min), and **K** is the Langmuir constant (L/mol). This equation can be simplified to the following pseudo-first-order expression when the concentration of reagent being reacted is too low [62]:

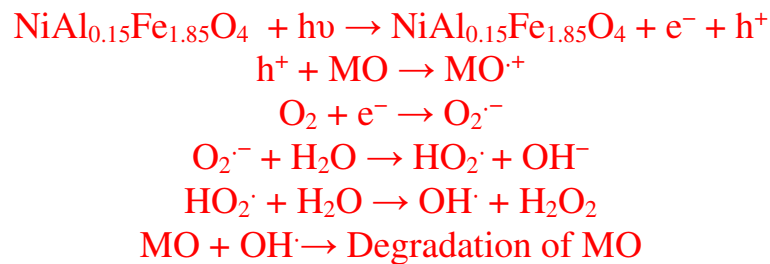
$$r = -dc/dt = kapp A \quad [6]$$

Integrating Eq. [6] results in:

$$\ln (A_t/A_0) = k_{app} t \quad [7]$$

Where k_{app} is the pseudo-first-order rate constant (L/min), t is the irradiation time (min), A_t and A_0 are dye concentrations (mol/L) at instants t and $t = 0$, respectively, [63]. To explore the order of photocatalytic reactions, plots $\ln (A_t/A_0) = f(\text{time})$. By considering the linear relation between $\ln (A_t/A_0)$ with time and negative slope of them, it can be said that these reactions were first-order (Fig. 10c).

The mechanism of photocatalytic activity of synthesized compounds for example $\text{NiAl}_{0.15}\text{Fe}_{1.85}\text{O}_4$ nanoparticles in the degradation of methyl orange (MO) dye is given below [64-68]:



4. Conclusion

In summary, Al-substituted nickel ferrite have been successfully prepared via a facile low-cost co-precipitation method. The TGA showed three mass losses, whereas DTA resulted in three endothermic peaks. The Rietveld refined XRD studies clearly showed the formation of single phase spinel structure. The lattice parameter is found to decrease with increasing aluminum content. TEM and SEM observations indicate cubic-shaped nanoparticles of $(\text{NiAl}_x\text{Fe}_{2-x}\text{O}_4)$. The crystalline particle size was found that in the range of 28 - 36 nm. FT-IR spectroscopy study shows 2 main metal oxygen bonds (Fe-O and M-O) at in the range of 400-600 cm^{-1} confirming the creation of single phase spinel ferrite. The Raman spectra shows five Raman active modes ($A_{1g} + E_g + 3T_{2g}$) which are expected in the spinel structure and Raman spectra has a very good agreement with reported data. In addition, the optical study showed that the

compounds have an optical band gap between 1.60 and 1.89 eV. Mössbauer spectra elucidate the nature of the phases and cation distribution. From the hysteresis loop, it is clear that the prepared samples can be control, for the $(\text{NiAl}_x\text{Fe}_{2-x}\text{O}_4)$ nano-ferrites. Furthermore, the photocatalytic activities of $\text{NiAl}_x\text{Fe}_{2-x}\text{O}_4$ nanoparticles were evaluated by studying the photodegradation of MO dye as model organic pollutant. The best photocatalytic activity was reached with the $\text{NiAl}_{0.15}\text{Fe}_{1.85}\text{O}_4$ sample due to lower crystallite size and improved light harvesting capability.

Acknowledgments

The present work was supported by the Research Funds of Electrochemistry, Materials and Environment Research Unit UREME (UR17ES45), Faculty of Sciences Gabes University, Tunisia and Structures, Properties and Modeling of Solids (SPMS) Laboratory, University Paris-Saclay, France.

References

- [1] J.C. Love, L.A. Estroff, J.K. Kriebel, R.G. Nuzzo, G.M. Whitesides, Self-assembled monolayers of thiolates on metals as a form of nanotechnology, *Chem. Rev.* 105 (2005) 1103–1169.
- [2] S. Nie, Y. Xing, G.J. Kim, J.W. Simons, Nanotechnology applications in cancer, *Annu. Rev. Biomed. Eng.* 9 (2007) 257–288.
- [3] M.C. Daniel, D. Astruc, Gold nanoparticles: assembly, supramolecular chemistry, quantum-size-related properties, and applications toward biology, catalysis, and nanotechnology, *Chem. Rev.* 104 (2004) 293–346.
- [4] M. N. Ashiq, S. Saleem, and M. A. Malana, Physical, electrical and magnetic properties of nanocrystalline Zr–Ni doped Mn-ferrite synthesized by the coprecipitation method, *Journal of Alloys and Compounds.* 486 (2009) 640-644.
- [5] M. Anupama, N. Srinatha, S. Matteppanavar, B. Angadi, B. Sahoo, and B. Rudraswamy, Effect of Zn substitution on the structural and magnetic properties of nanocrystalline NiFe₂O₄ ferrites, *Ceramics International.* 44 (2017) 4946-4954.
- [6] V. Sudheesh, N. Thomas, N. Roona, P. Baghya, and V. Sebastian, Synthesis, characterization and influence of fuel to oxidizer ratio on the properties of spinel ferrite (MFe₂O₄, M= Co and Ni) prepared by solution combustion method, *Ceramics International.* 43 (2017) 15002-15009.
- [7] L. Neel, Antiferromagnetism and Ferrimagnetism, *Proc. Phys. Soc. Lond.* A65 (1948) 869-885.
- [8] Gerald F. Dionne, A review of ferrites for microwave applications, *Proceedings of the IEEE.* 63 (1975) 777 – 789.
- [9] A. Lassoued, M.S. Lassoued, B. Dkhil, S. Ammar and A. Gadri, Improved photocatalytic activities of CuxCo_{0.5-x}Ni_{0.5}Fe₂O₄ nanoparticles through co-precipitation method in

degrading methylene blue, *Physica E: Low-dimensional Systems and Nanostructures*, 101 (2018) 29-37.

[10] J. L. Snoek, Magnetic and electrical properties of the binary systems $\text{MO} \cdot \text{Fe}_2\text{O}_3$, *Physica*. 3 (1936) 463-483.

[11] J. L. Snoek, *New developments in ferromagnetic materials*, Amsterdam, Elsevier. (1947).

[12] K. Kombaiah, J. Judith Vijaya, L. John Kennedy, M. Bououdina, K. Kaviyarasu, R. Jothi Ramalingam, Murugan A. Munusamy, Abdullah A. Alarfaj, Effect of Cd^{2+} concentration on ZnFe_2O_4 nanoparticles on the structural, optical and magnetic properties, *Optik-International Journal for Light and Electron Optics*. 135 (2017) 190-199.

[13] R.S. Pandav, R.P. Patil, S.S. Chavan, I.S. Mulla, P.P. Hankare, Magneto-structural studies of sol-gel synthesized nanocrystalline manganese substituted nickel ferrites, *J. Magn. Magn Mater.* 417 (2016) 407–412.

[14] X. Wang, S. Zhang, M. Shao, J. Huang, X. Deng, P. Hou, X. Xu, Fabrication of $\text{ZnO}/\text{ZnFe}_2\text{O}_4$ Hollow Nanocages Through Metal Organic Frameworks Route with Enhanced Gas Sensing Properties, *Journal of Sensors and Actuators B: Chemical*, 251 (2017) 27-33.

[15] M.A. Khan, Mu Islam, M.A. Iqbal, M. Ahmad, M.F. Din, G. Murtaza, I. Ahmad, M. F. Warsi, Magnetic, ferromagnetic resonance and electrical transport study of $\text{Ni}_{1-x}\text{TbxFe}_2\text{O}_4$ spinel ferrites, *Ceram. Int.* 40 (2014) 3571–3577.

[16] M.Y. Lodhi, K. Mahmood, A. Mahmood, H. Malik, M.F. Warsi, I. Shakir, M. Asghar, M.A. Khan, New $\text{Mg}_{0.5}\text{Co}_x\text{Zn}_{0.5-x}\text{Fe}_2\text{O}_4$ nano-ferrites: Structural elucidation and electromagnetic behavior evaluation, *Current Applied Physics*, 14 (2014) 716-720.

[17] J. Zhu, D. Xiao, Lo Jing, X. Yang, Y. Wu, Characterization of FeNi_3 alloy in Fe–Ni–O system synthesized by citric acid combustion method, *Scripta Mater.* 54 (2006) 109-113.

- [18] N. Rezlescu, N. Iftimie, E. Rezlescu, C. Doroftei, and P.D. Popa, Semiconducting gas sensor for acetone based on the grained nickel ferrite, *Sensors and Actuators B*. 114 (2006) 427–432.
- [19] M.K. Shobana. Sankar, Structural, thermal and magnetic properties of $\text{Ni}_{1-x}\text{Mn}_x\text{Fe}_2\text{O}_4$ nanoferrites. *J. Magn.Magn.Mater.* 321 (2009) 2125-2128.
- [20] L.Guo, X.Shen, X.Meng, Y.Feng, Effect of Sm^{3+} ions doping on structure and magnetic properties of nanocrystalline NiFe_2O_4 fibers, *J. Alloys Compd.* 490 (2010) 301–306.
- [21] H. Li, H.Z. Wu, G.X. Xiao, Effects of synthetic conditions on particle size and magnetic properties of NiFe_2O_4 , *Powder Technol*, 198 (2010) 157–166.
- [22] J.M. Yang, W.J. Tsuo, F.S. Yen, Preparation of ultrafine nickel ferrite powders using mixed Ni and Fe tartrates, *J. Solid State Chem*, 145 (1999) 50–57.
- [23] L. Chena, H. Dai, Y. Shen, J. Bai, Composition and film thickness effects on microstructure and magnetic properties of ordered L10-structured $\text{Fe}_{100-x}\text{Pt}_x$ films, *J. Alloys Compd*, 491 (2010) 33–38.
- [24] N.Z. Bao, L.M. Shen, Y.H. Wang, P. Padhan, A. Gupta, A Facile Thermolysis Route to Monodisperse Ferrite Nanocrystals, *J. Am. Chem. Soc*, 129 (2007) 12374–12375.
- [25] S.M. Patange, Sagar E. Shirsath, S.S. Jadhav, K.S. Lohar, D.R. Mane, K.M. Jadhav, Rietveld refinement and switching properties of Cr^{3+} substituted NiFe_2O_4 ferrites, *Mater. Lett*, 64 (2010) 722–724.
- [26] W.B. Cross, L. Affleck, M.V. Kuznetsov I. P. Parkin and Q. A. Pankhurst, Self-propagating high-temperature synthesis of ferrites MFe_2O_4 ($\text{M} = \text{Mg}, \text{Ba}, \text{Co}, \text{Ni}, \text{Cu}, \text{Zn}$); reactions in an external magnetic field, *J. Mater. Chem*, 9 (1999) 2545–2552.
- [27] C. Liu, B. Zou, A.J. Rondinone and Z. J. Zhang, Reverse micelle synthesis and characterization of superparamagnetic MnFe_2O_4 spinel ferrite nanocrystallites, *J. Phys. Chem. B*, 104 (2000) 1141–1145.

- [28] T. Hirai, J. Kobayashi, I. Komasaawa, Preparation of acicular ferrite fine particles using an emulsion liquid membrane system, *Langmuir*, 15 (1999) 6291–6298.
- [29] P. Sivakumar, R. Ramesh, A. Ramanand, S. Ponnusamy, C. Muthamizhchelvan, Synthesis and characterization of NiFe₂O₄ nanosheet via polymer assisted co-precipitation method, *Mater. Lett*, 65 (2011) 483–485.
- [30] P. Sivakumar, R. Ramesh, A. Ramanand, S. Ponnusamy, C. Muthamizhchelvan, Preparation and properties of nickel ferrite (NiFe₂O₄) nanoparticles via sol–gel auto-combustion method, *Materials Research Bulletin*, 46 (2011) 2204-2207.
- [31] I. Maghsoudi, H. Shokrollahi, M.J. Hadianfard, J. Amighian, Synthesis and characterization of NiAl_xFe_{2-x}O₄ magnetic spinel ferrites produced by conventional method, *Powder Technology*. 235 (2013) 110–114
- [32] V. Pallai and D. O Shah, Synthesis of High-Coercivity Cobalt Ferrite Particles Using Water-in-Oil Microemulsions, *Journal of Magnetism and Magnetic Materials*, 163 (1996) 243-248.
- [33] B. Rajesh Babu, M.S.R. Prasad, K.V. Ramesh, Effect on structural and magnetic properties of aluminum substituted Ni Zn nanoferrite system prepared via citrate-gel route, *Inter. J. Mod. Phys. B*, 29 (2015) 1550032.
- [34] N. Bouhadouza, A. Rais, S. Kaoua, M. Moreau, K.Taibi, A. Addou, Structural and Vibrational Studies of NiAl_xFe_{2-x}O₄ Ferrites (0 ≤ x ≤ 1), *Ceramics International*. 41 (2015) 11687–11692.
- [35] A. Lassoued, M.S. Lassoued, B. Dkhil, S. Ammar and A. Gadri, Synthesis, structural, morphological, optical and magnetic characterization of iron oxide (α-Fe₂O₃) nanoparticles by precipitation method: Effect of varying the nature of precursor, *Physica E: Low-dimensional Systems and Nanostructures*, 97 (2018) 328-334.

- [36] A. Lassoued, M.S. Lassoued, B. Dkhil, A. Gadri, S. Ammar, Synthesis, structural, optical and morphological characterization of hematite through the precipitation method: Effect of varying the nature of the base, *Journal of Molecular Structure*. 1141 (2017) 99-106.
- [37] A. Lassoued, B. Dkhil, A. Gadri, S. Ammar, Control of the shape and size of iron oxide (α -Fe₂O₃) nanoparticles synthesized through the chemical precipitation method, *Results in Physics*. 7 (2017) 3007-3015.
- [38] A. Lassoued, M. S. Lassoued, B. Dkhil, A. Gadri, S. Ammar, Structural, optical and morphological characterization of Cu-doped α -Fe₂O₃ nanoparticles synthesized through co-precipitation technique, *Molecular Structure*. 1148 (2017) 276-281.
- [39] H. Rietveld, A profile refinement method for nuclear and magnetic structures, *Journal of Applied Crystallography*, 2 (1969) 65–71.
- [40] Zhenxing Yue, Ji Zhou, Longtu Li, Xiaohui Wang, Zhilun Gui, Effect of Copper on the Electromagnetic Properties of Mg-Zn-Cu Ferrites Prepared by Sol-Gel Auto-Combustion Method, *Mater. Sci. Eng. B86* (2001) 64-69.
- [41] I. Maghsoudi, H. Shokrollahi, M.J. Hadianfard, J. Amighian, Synthesis and characterization of NiAl_xFe_{2-x}O₄ magnetic spinel ferrites produced by conventional method, *Powder Technology*, 235 (2013) 110-114.
- [42] T.C. Verma, R.G. Goel, Mendiratta, R.G. Gupta, High-resistivity nickel-zinc ferrites by the citrate precursor method, *J. Magn. Magn. Mater*, 192 (1999) 271-276.
- [43] A. Lassoued, M. S. Lassoued, F. Karolak, S. García-Granda, B. Dkhil, S. Ammar, A. Gadri, Synthesis, structural, optical, morphological and magnetic characterization of copper substituted nickel ferrite (Cu_xNi_{1-x}Fe₂O₄) through co-precipitation method, *Materials Science: Materials in Electronics*. 28 (2017) 18480-18488.
- [44] A. Lassoued, M.S. Lassoued, B. Dkhil, S. Ammar and A. Gadri, Nanocrystalline Ni_xCo(0.5-x)Zn_{0.5}Fe₂O₄ ferrites: fabrication through co-precipitation route with enhanced

structural, magnetic and photo-catalytic activity, *Journal of Materials Science: Materials in Electronics*. 29 (2018) 7333-7344.

[45] M.H.R. Khan, A.K.M. Akther Hossain, Reentrant spin glass behavior and large initial permeability of $\text{Co}_{0.5-x}\text{Mn}_x\text{Zn}_{0.5}\text{Fe}_2\text{O}_4$, *J. Magn. Magn. Mater.*, 324 (2012) 550-558.

[46] J. Chandradass, A. H. Jadhav, K. H. Kim, H. Kim, Influence of processing methodology on the structural and magnetic behavior of MgFe_2O_4 nanopowders, *J. Alloys Comp.*, 517 (2012) 164–169.

[47] K. Kombaiah, J. Judith Vijaya, L. John Kennedy, M. Bououdina, K. Kaviyarasu, R. Jothi Ramalingam, Hamad A. Al-Lohedan, Murugan A. Munusamy. A Green approach: synthesis, characterization and opto-magnetic properties of $\text{Mg}_x\text{Mn}_{1-x}\text{Fe}_2\text{O}_4$ spinel nanoparticles. *Journal of Materials Science: Materials in Electronics*. 28 (2017) 10321-10329.

[48] P. Yaseneva, M. Bowker, G. Hutchings, Structural and magnetic properties of Zn-substituted cobalt ferrites prepared by co-precipitation method, *Phys. Chem. Chem. Phys.* 13 (2011) 18609–18614.

[49] A. Lassoued, M. Ben hassine, F. Karolak, B. Dkhil, S. Ammar, A. Gadri, Synthesis and magnetic characterization of Spinel ferrites MFe_2O_4 (M = Ni, Co, Zn and Cu) via chemical co-precipitation method, *Materials Science: Materials in Electronics*. 28 (2017) 18857-18864.

[50] D. Varshney, K. Verma, A. Kumar, Substitutional effect on structural and magnetic properties of $\text{A}_x\text{Co}_{1-x}\text{Fe}_2\text{O}_4$ (A = Zn, Mg and x = 0.0, 0.5) ferrites, *J.Mol. Struct.*, 1006 (2011) 447–452.

[51] R. Branek, H. Kisch, Tuning the optical and photoelectrochemical properties of surface-modified TiO_2 , *Photochemical and Photobiological Sciences*, 7 (2008) 40-48.

[52] A. Lassoued, M.S. Lassoued, B. Dkhil, S. Ammar and A. Gadri, Synthesis, photoluminescence and Magnetic properties of iron oxide ($\alpha\text{-Fe}_2\text{O}_3$) nanoparticles through

precipitation or hydrothermal methods, *Physica E: Low-dimensional Systems and Nanostructures*, 101 (2018) 212-219.

[53] M.S. Lassoued, A. Lassoued, M.S. M. Abdelbaky, S. Ammar, A. Gadri, A. Ben Salah, S. García-Granda, Influence of iron doping on the photocatalytic activity of nanocrystalline TiO₂ particles fabricated by ultrasound method for enhanced degradation of organic dye. *Materials Science: Materials in Electronics*. 29 (2018) 6019-6031.

[54] A. Lassoued, M.S. Lassoued, B. Dkhil, S. Ammar, A. Gadri, Synthesis and characterization of Ni-doped α -Fe₂O₃ nanoparticles through co-precipitation method with enhanced photocatalytic activities, *Materials Science: Materials in Electronics*. 29 (2018) 5726-5737.

[55] A. Lassoued, M.S. Lassoued, B. Dkhil, S. Ammar, A. Gadri, Photocatalytic degradation of methyl orange dye by NiFe₂O₄ nanoparticles under visible irradiation: effect of varying the synthesis temperature, *Journal of Materials Science: Materials in Electronics*. 29 (2018) 7057-7067.

[56] J.I. Pankov, *Optical Processes in Semiconductors*, Prentice-Hall Inc., New Jersey, 31 (1971) 34-86.

[57] M. Mohammadikish, Hydrothermal synthesis, characterization and optical properties of ellipsoid shape α -Fe₂O₃ nanocrystals, *Ceramics International*, 40 (2014) 1351–1358.

[58] A. Ahlawat, V.G. Sathe, V.R. Reddy, A. Gupta, Mossbauer, Raman and X-ray diffraction studies of superparamagnetic NiFe₂O₄ nanoparticles prepared by sol–gel auto-combustion method, *Journal of Magnetism and Magnetic Materials*. 323 (2011) 2049–2054.

[59] N. Singh, A. Agarwal, S. Sanghi, P. Singh, Synthesis, microstructure, dielectric and magnetic properties of Cu substituted NiLi ferrites, *J. Magn. Magn. Mater*, 323 (2011) 486-492.

- [60] W. Ben Soltan, M.S. Lassoued, S. Ammar, T. Toupance, Vanadium doped SnO₂ nanoparticles for photocatalytic degradation of methylene blue, *J. Mater. Sci.: Mater. Electron.* 28 (2017) 15826
- [61] C. Sahoo, AK. Gupta, IM. Sasidharan Pillai, Heterogeneous photocatalysis of real textile wastewater: Evaluation of reaction kinetics and characterization, *Journal of Environmental Science and Health.* 47 (2012) 2109–2119.
- [62] J. M. Herrmann, Heterogeneous photocatalysis Fundamentals and applications to the removal of various types of aqueous pollutants, *Catal. Today.* 53 (1999) 115-129.
- [63] F. Motahari, M.R. Mozdianfard, F. Soofivand, M. Salavati-Niasari, NiO nanostructures: synthesis, characterization and photocatalyst application in dye wastewater treatment, *RSC Adv.* 4 (2014) 27654–27660.
- [64] M.S. Lassoued, A. Lassoued, S. Ammar, A. Gadri, A. Ben Salah, S. García-Granda, Synthesis and characterization of Co-doped nano-TiO₂ through co-precipitation method for photocatalytic activity, *J. Mater. Sci.: Mater. Electron.* 28 (2018) 8914–8922
- [65] M. Sivachidambaram, J. Judith Vijaya, K. Kaviyarasu, L. John Kennedy, Hamad A. Al-Lohedan and R. Jothi Ramalingam, A novel synthesis protocol for Co₃O₄ nanocatalysts and their catalytic applications, *RSC Advances.* 7 (2017) 38861-38870.
- [66] P Iyyappa Rajan, J Judith Vijaya, S K Jesudoss, K Kaviyarasu, L John Kennedy, R Jothiramalingam, Hamad A Al-Lohedan and Mansoor-Ali Vaali-Mohammed, Green-fuel-mediated synthesis of self-assembled NiO nano-sticks for dual applications—photocatalytic activity on Rose Bengal dye and antimicrobial action on bacterial strains, *Materials Research Express.* 4 (2017) 085030.
- [67] SK. Jesudoss, JJ. Vijaya, LJ. Kennedy, PL. Rajan, HA. Al-Lohedan, RJ. Ramalingam, K. Kaviyarasu, M. Bououdina, Studies on the efficient dual performance of Mn¹⁻

xNi_xFe_{2-x}O₄ spinel nanoparticles in photodegradation and antibacterial activity. *J Photochem Photobiol B.* 165 (2016) 121-132.

[68] S. K. Jesudoss, J. Judith Vijaya, P. Iyyappa Rajan, K. Kaviyarasu, M. Sivachidambaram, L. John Kennedy, H A. Al Lohedan and R. Jothiramalingam, High performance multifunctional green Co₃O₄ spinel nanoparticles: photodegradation of textile dye effluents, catalytic hydrogenation of nitro-aromatics and antibacterial potential. *Photochemical & Photobiological Sciences.* 16 (2017) 766-778.

Table captions

Table 1. Results of the Rietveld refinement of the X-ray diffractograms and crystallite size (D_{XRD}) of the as-prepared samples

Table 2. The optical band gap of $\text{NiAl}_x\text{Fe}_{2-x}\text{O}_4$

Table 3. Mossbauer's parameters of $\text{NiAl}_x\text{Fe}_{2-x}\text{O}_4$ nanoparticles

Table 4. Magnetic properties of $\text{NiAl}_x\text{Fe}_{2-x}\text{O}_4$ nanoparticles at room temperature

Figure captions

Fig. 1. TGA and DTA curves for the as-prepared ferrite $\text{NiAl}_{0.05}\text{Fe}_{1.95}\text{O}_4$

Fig. 2. The Rietveld analysis of X-ray diffraction patterns for $\text{NiAl}_x\text{Fe}_{2-x}\text{O}_4$ ferrites with different amounts of aluminum substitution: (a) $x=0.00$, (b) $x=0.05$, (c) $x=0.10$ and (d) $x=0.15$.

Fig. 3a. Shift in 2θ with increasing Al concentration.

Fig. 3b. Variation of lattice parameter (a) and the average crystallite size (D_{XRD}) with Al concentration for $\text{NiAl}_x\text{Fe}_{2-x}\text{O}_4$ with $x = (0.00, 0.05, 0.10, \text{ and } 0.15)$

Fig. 4a. TEM images of the prepared samples

Fig. 4b. SEM images of the prepared samples

Fig. 5. FT-IR spectra of synthesized compounds calcined at $700\text{ }^\circ\text{C}$

Fig. 6. Raman spectra of the nanoparticles $\text{NiAl}_x\text{Fe}_{2-x}\text{O}_4$

Fig. 7a. Tauc plot obtained from UV-Vis DRS spectra of $\text{NiAl}_x\text{Fe}_{2-x}\text{O}_4$ synthesized from the chemical co-precipitation method

Fig. 7b. The variation of the band gap energy (E_g) as a function of Al concentration

Fig. 8. Mössbauer spectra of the samples

Fig. 9a. Hysteresis loops of the prepared ferrites at room temperature

Fig. 9b. The variation of the saturation magnetization (M_s) and the coercivity (H_c) values with varying aluminum substitution amounts

Fig. 10a. Photodegradation kinetics of MO dye in the presence of $\text{NiAl}_x\text{Fe}_{2-x}\text{O}_4$ nanoparticles

Fig. 10b. Bar diagram for the % degradation of MO dye in the presence of $\text{NiAl}_x\text{Fe}_{2-x}\text{O}_4$ nanoparticles

Fig. 10c. The pseudo first order kinetics of degradation of Methyl Orange dye

Figures :

Fig. 1

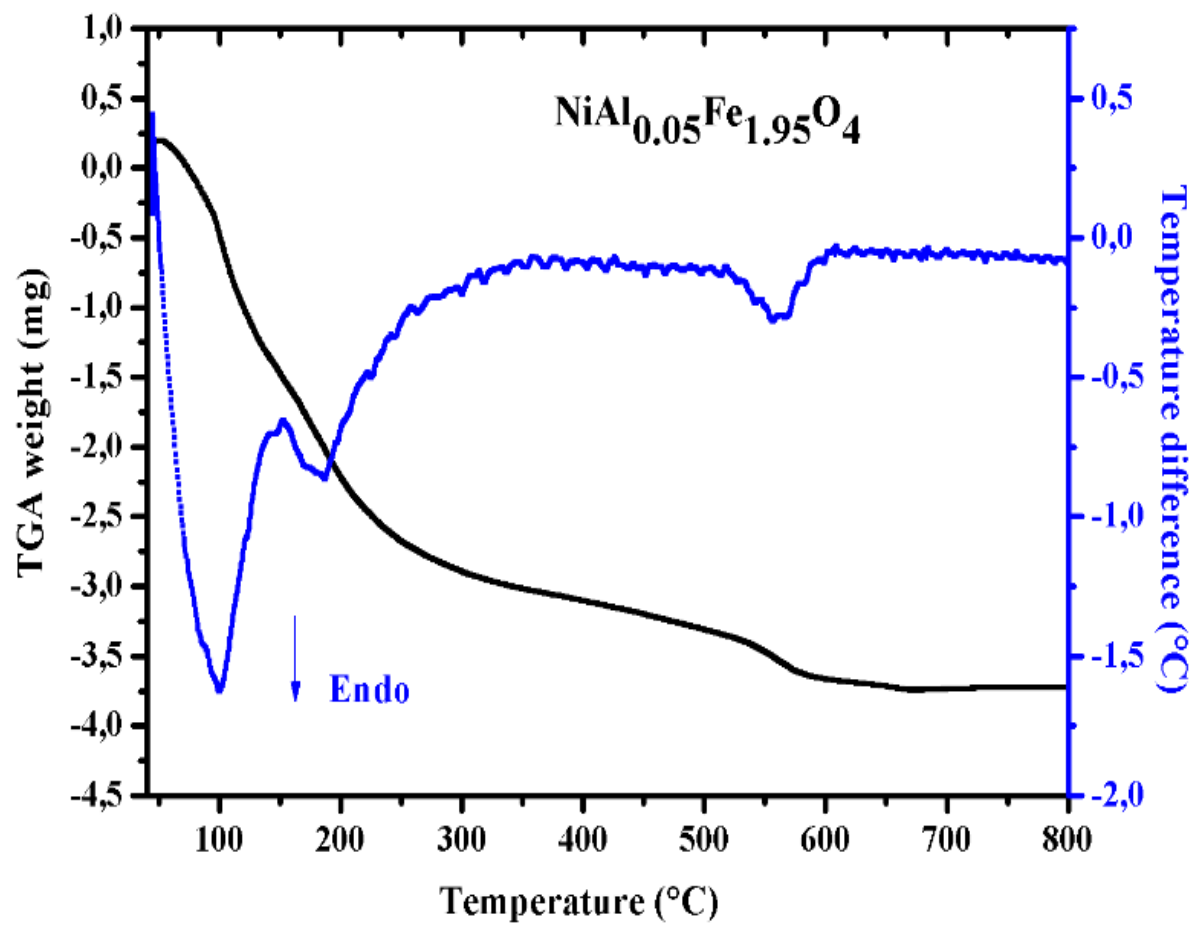


Fig. 2

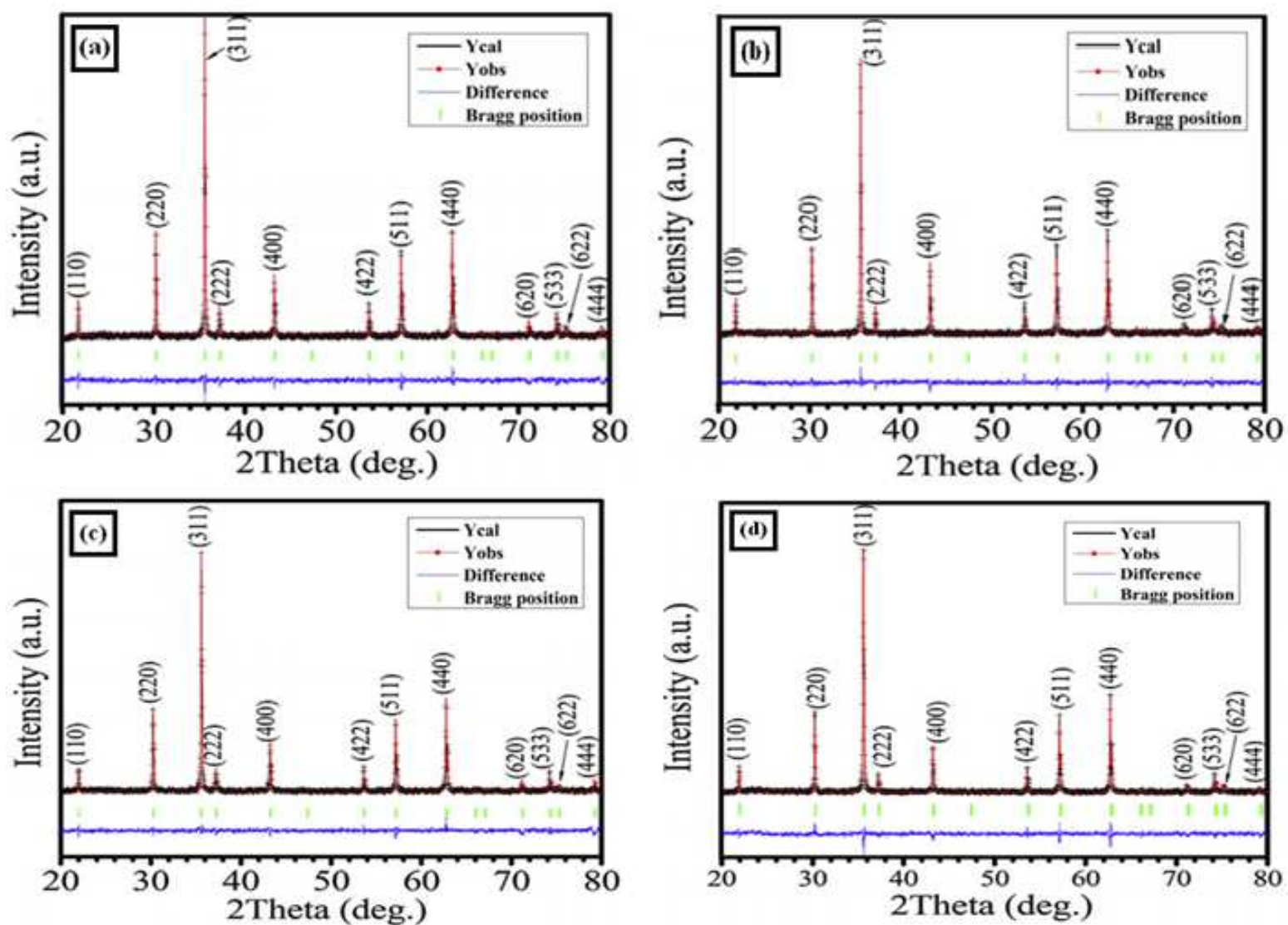


Fig. 3a

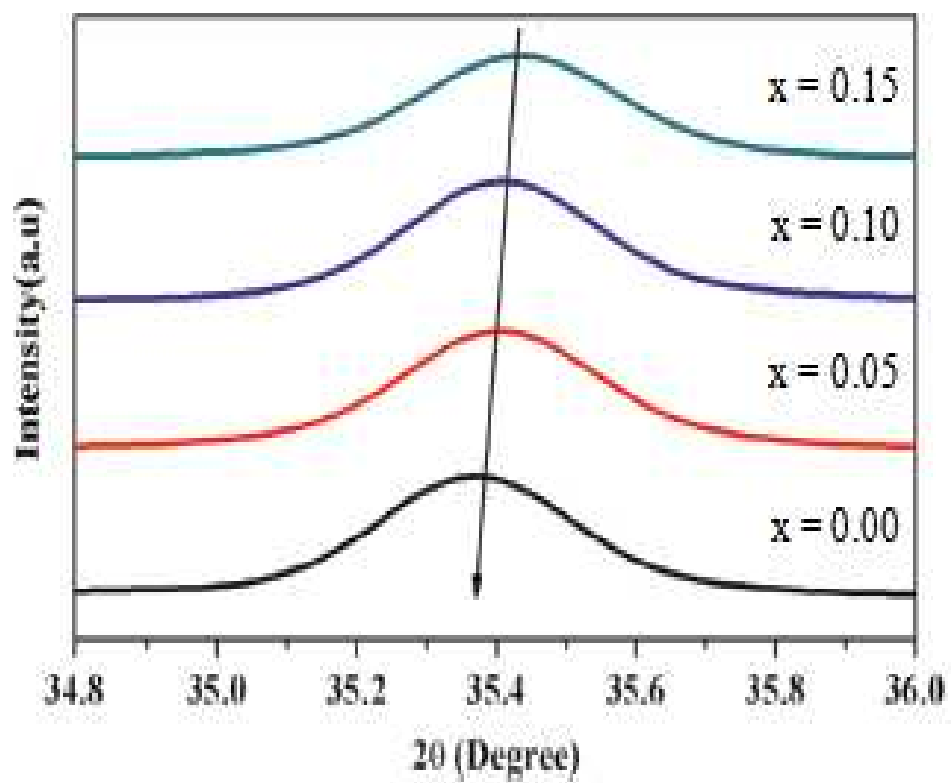


Fig. 3b

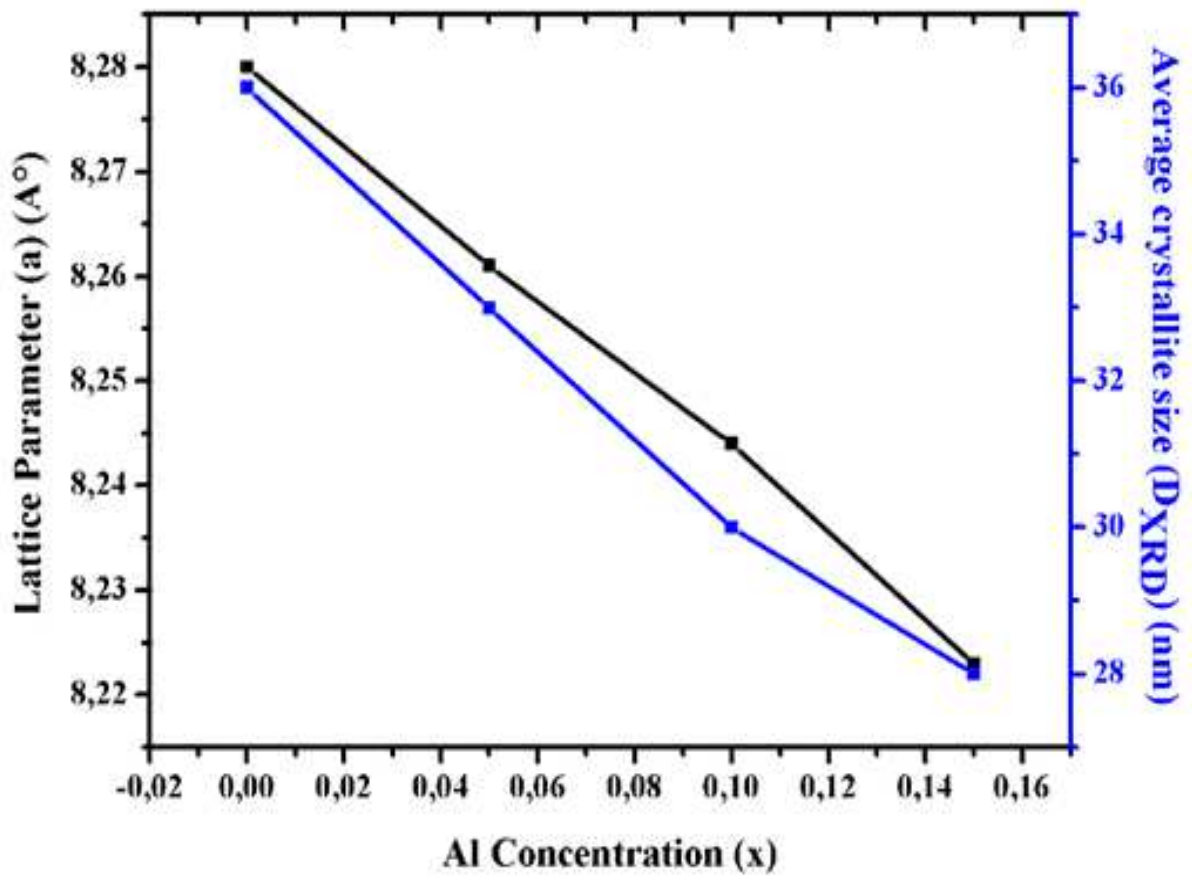


Fig. 4a

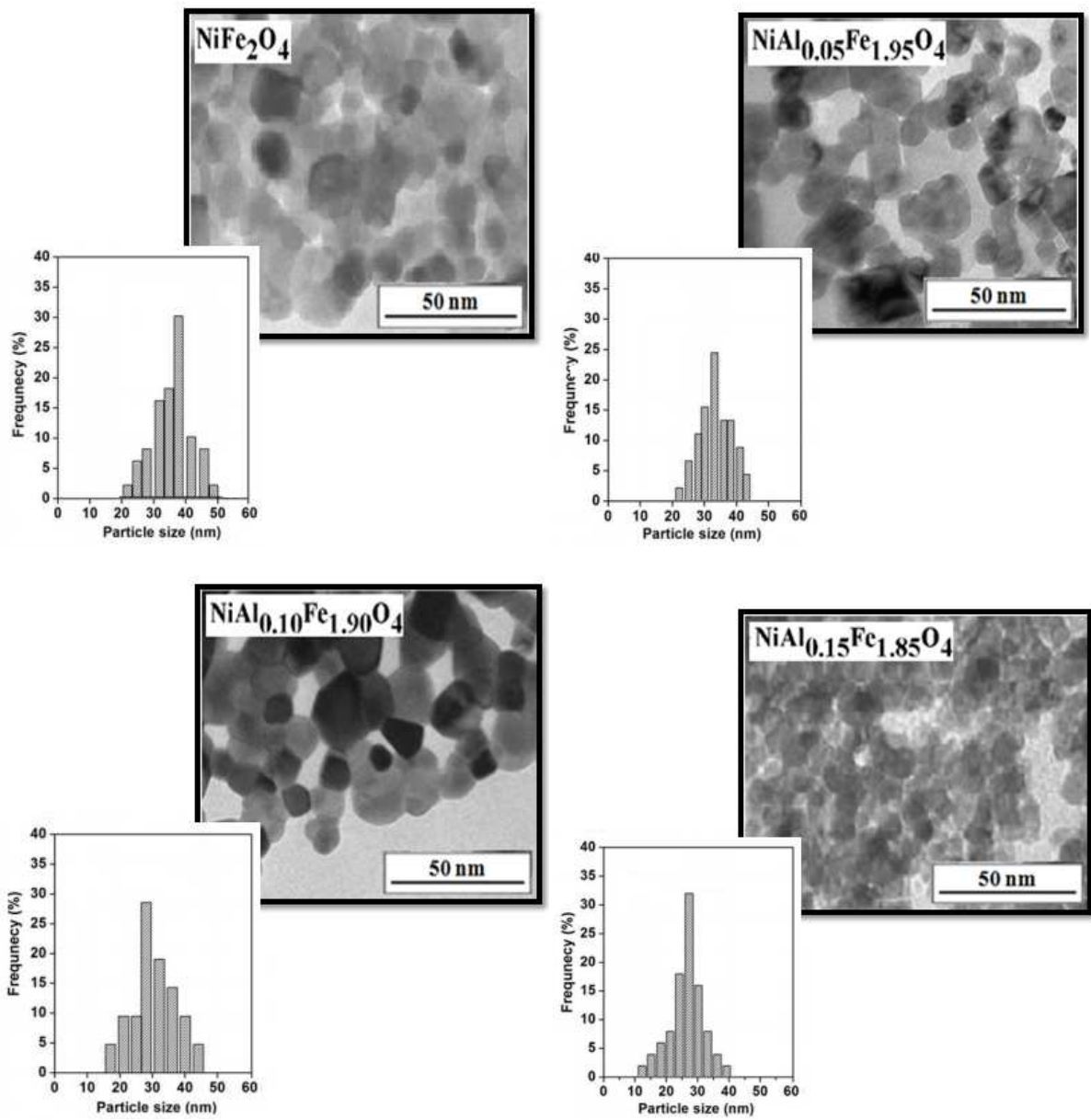


Fig. 4b

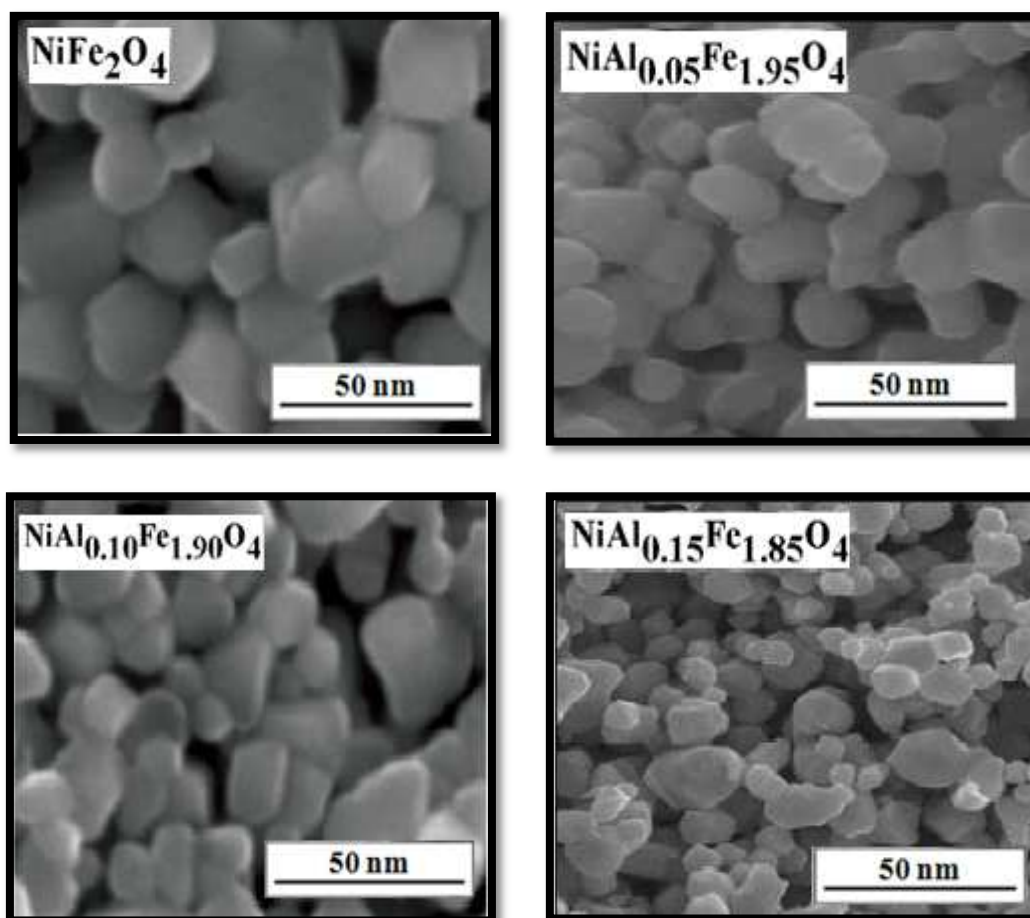


Fig. 5

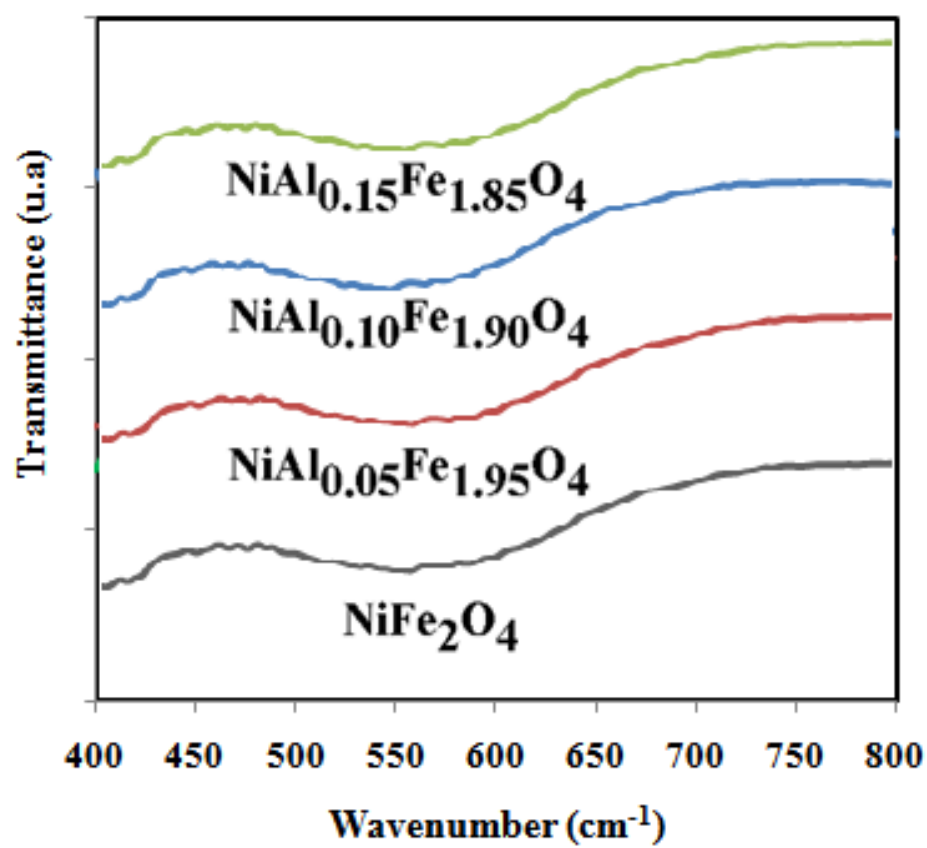


Fig. 6

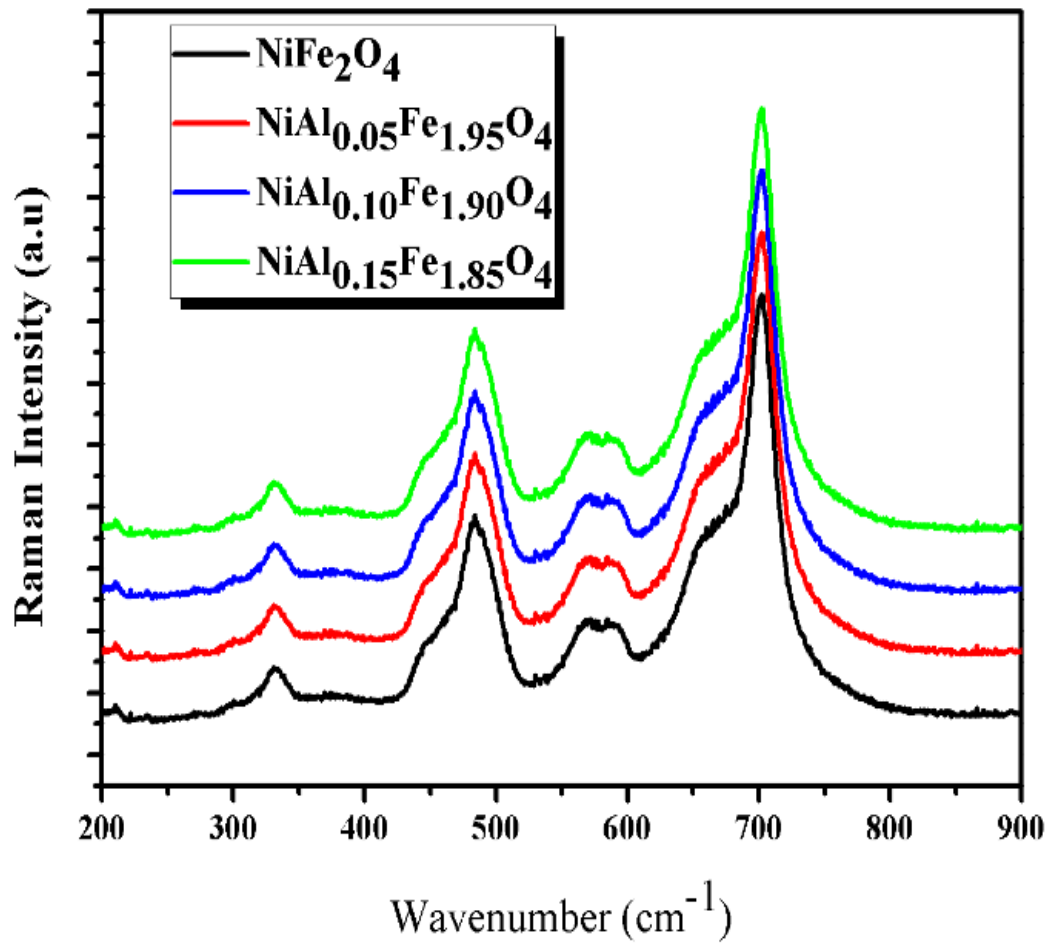


Fig. 7a

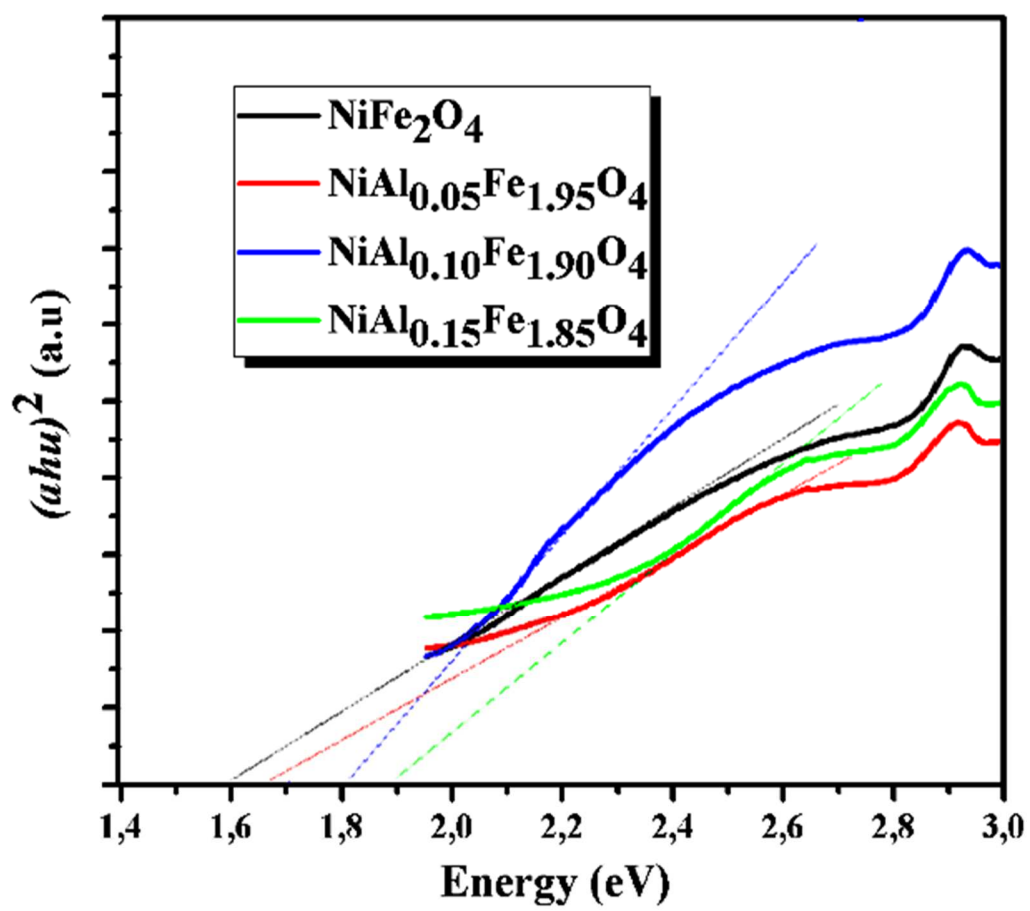


Fig. 7b

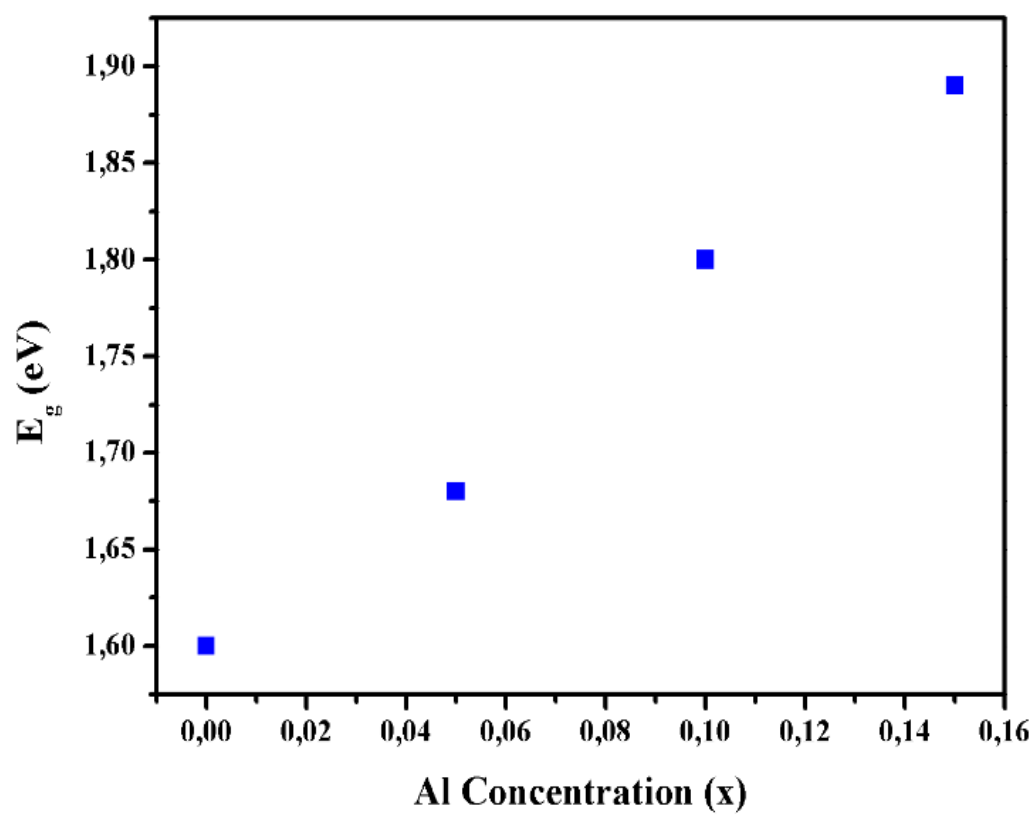


Fig. 8

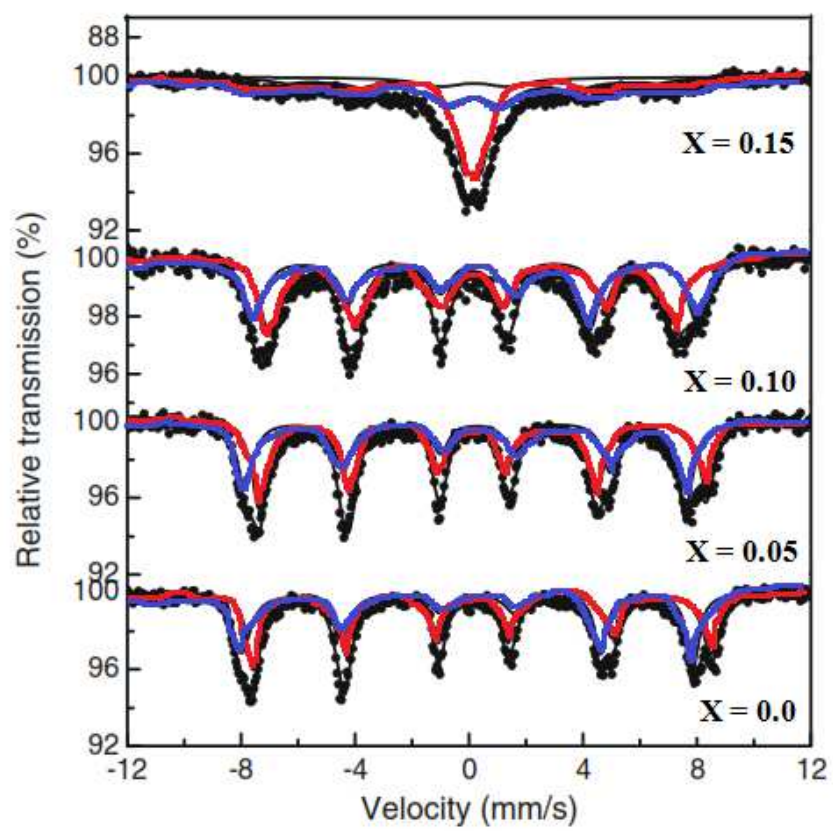


Fig. 9a

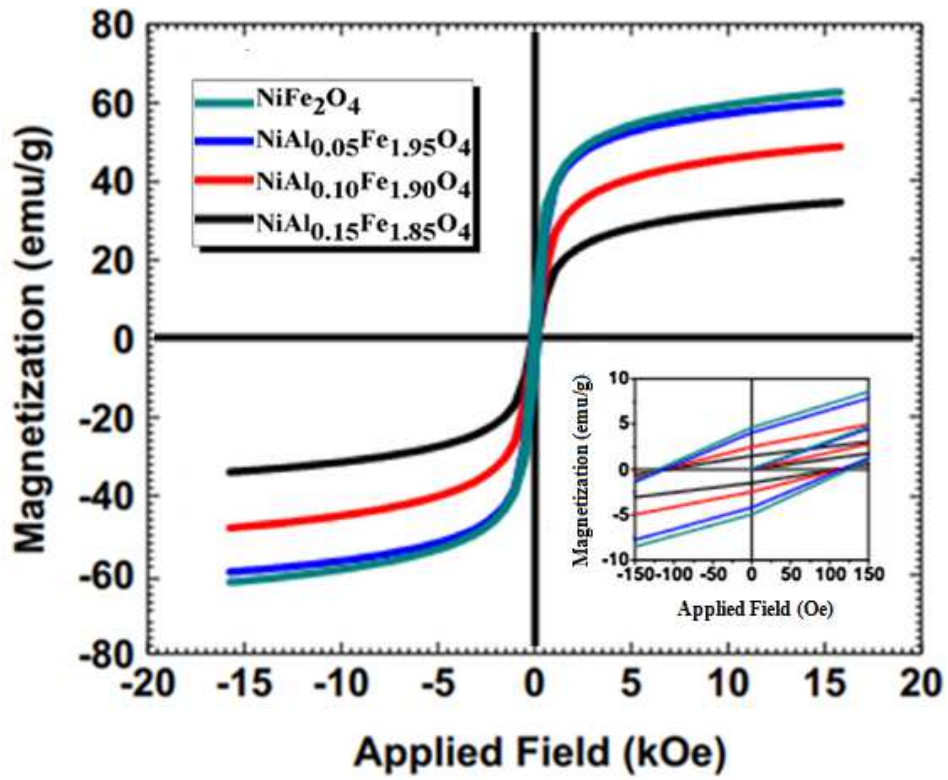


Fig. 9b

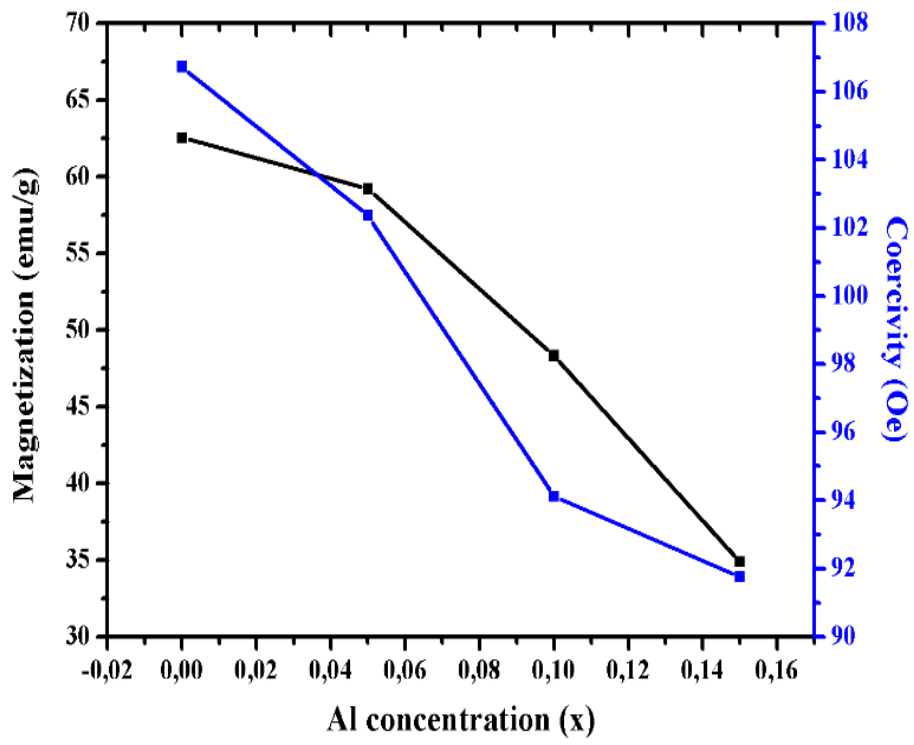


Fig. 10a

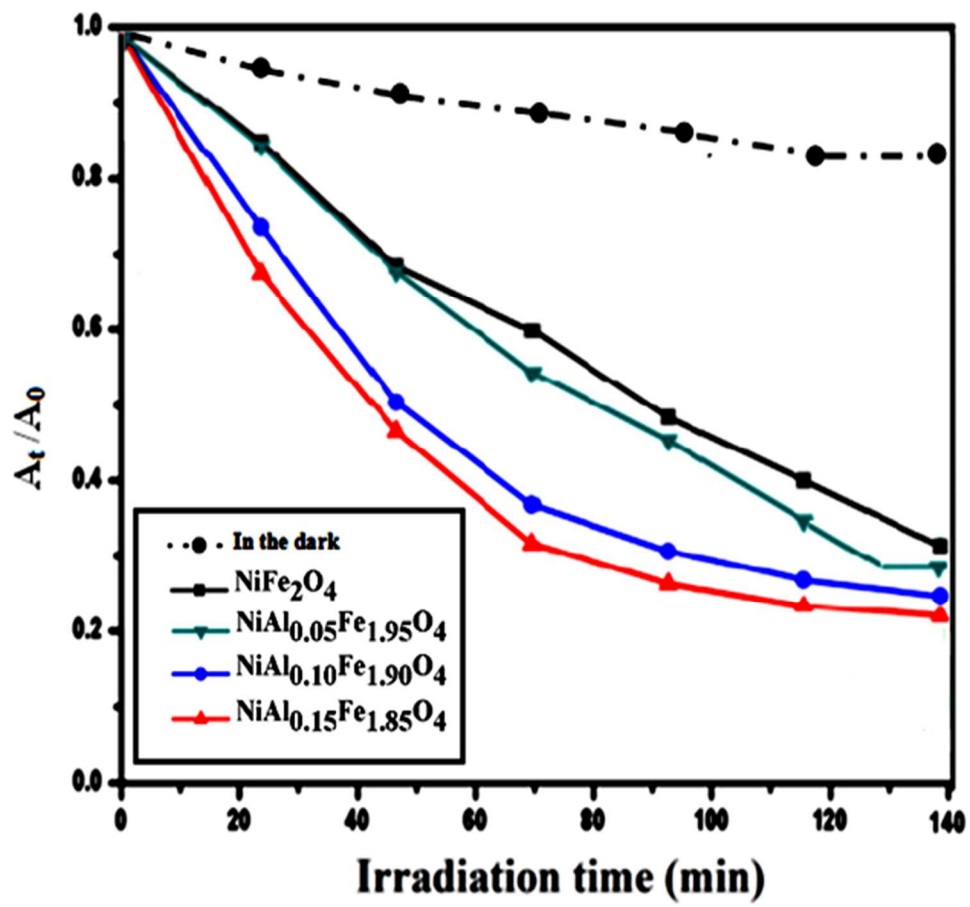


Fig. 10b

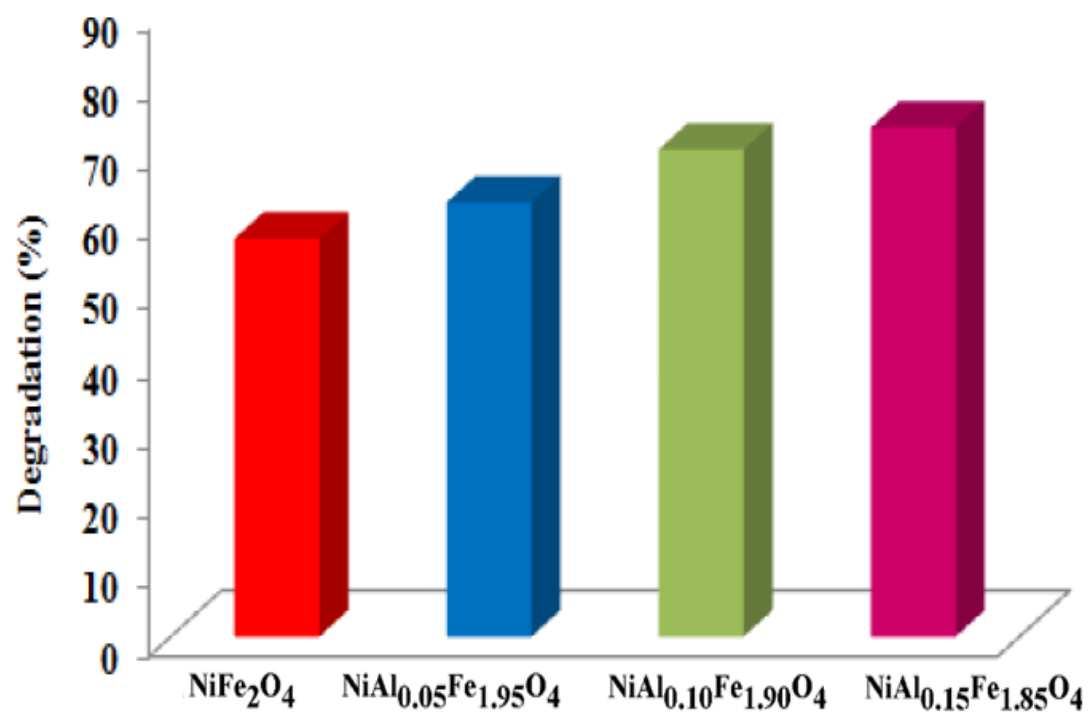
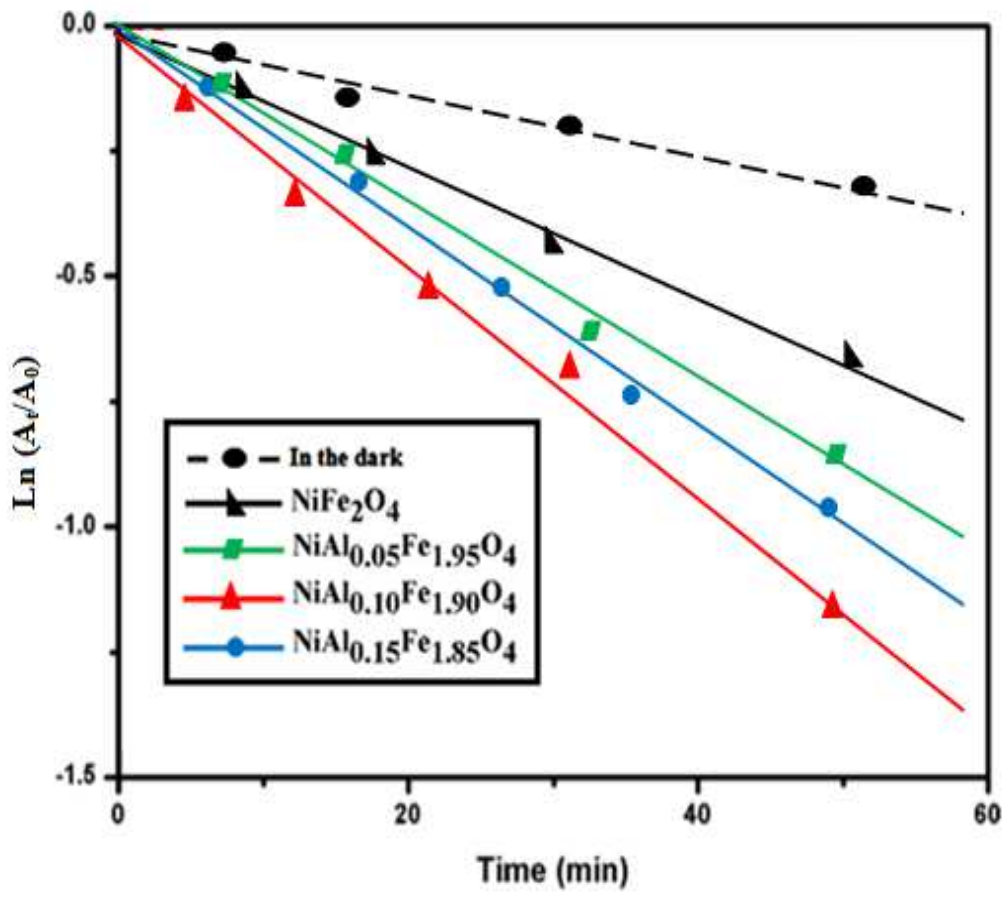


Fig. 10c



Table**Table 1**

Samples	Space group	a (Å)	V (Å³)	D_{XRD} (nm)	R_{wp}	R_p	χ²
NiFe₂O₄	Fd-3m	8.280	567.663	36	1.89	1.58	1.34
NiAl_{0.05}Fe_{1.95}O₄	Fd-3m	8.261	563.764	33	1.59	1.23	1.24
NiAl_{0.10k}Fe_{1.90}O₄	Fd-3m	8.244	560.291	30	2.01	1.59	1.59
NiAl_{0.15}Fe_{1.85}O₄	Fd-3m	8.223	556.696	28	1.45	1.38	1.08

Table 2

Samples	Optical band gap 'E_g' (eV)
NiFe₂O₄	1.60
NiAl_{0.05}Fe_{1.95}O₄	1.68
NiAl_{0.10}Fe_{1.90}O₄	1.80
NiAl_{0.15}Fe_{1.85}O₄	1.89

Table 3

x	Component	IS (mm/s)	QS (mm/s)	Hf (KOe)	HWHM (mm/s)	AREA (%)
0.15	Tetrahedral	0.21	0.02	379	0.85	40.8
	Octahedral	0.26	0.04	446	0.85	26.1
	Double	0.23	0.58	-	0.40	33.1
0.10	Tetrahedral	0.21	0.03	439	0.40	57.8
	Octahedral	0.33	0.01	481	0.41	42.2
0.05	Tetrahedral	0.24	0.02	464	0.31	55.1
	Octahedral	0.36	0.03	502	0.34	44.9
0.00	Tetrahedral	0.24	0.02	479	0.26	49.6
	Octahedral	0.37	0.01	511	0.39	50.4
Errors	-	±0.01	±0.01	±1	±0.01	±0.2

IS is the isomer shift, **QS** is the quadrupole splitting, **Hf** is the magnetic hyperfine field, **HWHM** is the half width at half maximum, and **AREA** is the absorption area.

Table 4

Samples	M_s (emu/g)	M_r (emu/g)	H_c (Oe)
NiFe₂O₄	62.54	4.83	106.72
NiAl_{0.05}Fe_{1.95}O₄	59.21	4.07	102.36
NiAl_{0.10}Fe_{1.90}O₄	48.33	2.48	94.12
NiAl_{0.15}Fe_{1.85}O₄	34.87	1.21	91.76

Synthesis of Spinel ferrites $\text{NiAl}_x\text{Fe}_{2-x}\text{O}_4$ through co-precipitation method

